1 **First Direct Observational Evidence for Secondary Gravity Waves Generated by**
2 **Mountain Waves over the Andes**
3

4 **Masaru Kogure[1], Jia Yue[2,3], Takuji Nakamura[4,5], Lars Hoffmann[6], Sharon L. Vadas[7],**
5 **Yoshihiro Tomikawa[4,5], Mitsumu K. Ejiri[4,5], Diego Janches[2,3]**

6

7 [1]Department of Earth and Planetary Science, Kyushu University, 744 Motooka Nishi-ku,
8 Fukuoka, Japan

9 [2]NASA Goddard Space Flight Center, 8800 Greenbelt Rd, Greenbelt, MD, USA

10 [3]Catholic University of America, 620 Michigan Ave NE, Washington, DC, USA

11 [4]National Institute of Polar Research, 10-3, Midori-cho, Tachikawa-shi, Tokyo, Japan

12 [5]The Graduate University for Advanced Studies, SOKENDAI, 10-3, Midori-cho, Tachikawa-shi,
13 Tokyo, Japan

14 [6]Forschungszentrum Jülich, Wilhelm-Johnen-Straße, 52428 Jülich, Germany

15 [7]NorthWest Research Associates, 3380 Mitchell Lane, Boulder, CO, USA

16

17 Corresponding author: Masaru Kogure (kogure.masaru.695@m.kyushu-u.ac.jp)

18 **Key Points:**

19 • VIIRS captured nightglow concentric ring-like gravity waves in mesopause east of
20   Southern Andes during intense winter mountain wave event.

21 • Mountain waves observed by AIRS likely broke while the waves were propagating
22   upward and eastward.

23 • Concentric ring-like gravity waves captured by VIIRS were likely generated by a local
24   body force created by mountain wave breaking.
25

26 **Abstract**

27 A mountain wave with a significant brightness temperature amplitude and ~500 km horizontal
28 wavelength was observed over the Southern Andes on 24–25 July 2017 in AIRS/Aqua satellite
29 data. In the MERRA-2 reanalysis data, a mesoscale vortex-like pattern appeared to the west of
30 the Andes at 2 km, and the wind flowed over the Andes. VIIRS/Suomi-NPP did not detect the
31 mountain waves; however, it observed concentric ring-like waves in the nightglow emissions at
32 ~87 km with ~100 km wavelengths on the same night over and leeward of the Southern Andes.
33 A ray tracing analysis showed that the mountain waves propagated to the east of the Andes,
34 where concentric ring-like waves appeared while mountain waves broke. Therefore, the
35 concentric ring-like waves were likely secondary gravity waves generated by momentum
36 deposition that accompanied mountain wave breaking. These results provide the first direct
37 evidence for secondary gravity waves generated by momentum deposition.

38 **Plain Language Summary**
39 A recent model study (Vadas and Becker, 2019) showed that mountain waves created over the
40 Andes broke in the stratosphere and mesosphere, thereby depositing their momentum and
41 creating "secondary" gravity waves. These secondary waves then propagated into the lower
42 thermosphere and created high-order waves, some of which propagated to the upper
43 thermosphere. This vertical multistep coupling mechanism is likely important for creating
44 ionospheric disturbances in the F region. However, observational evidence supporting this
45 mechanism is lacking. The purpose of this study is to show observational evidence using data
46 from two satellite instruments: AIRS/Aqua and VIIRS/Suomi-NPP. AIRS captured a mountain
47 wave with a significant amplitude in the stratosphere over the Andes on 24-25 July 2017.
48 VIIRS/Suomi-NPP did not detect the mountain waves but instead observed concentric ring-like
49 gravity waves in the upper mesosphere on the leeward of the Andes. The concentric ring-like
50 structure is one of the features of secondary waves created from momentum deposition that
51 accompanies breaking gravity waves; thus, we conclude that the observed gravity waves were
52 likely secondary gravity waves. These observational results provide the first direct evidence for
53 secondary gravity waves generated by momentum deposition from breaking mountain waves and
54 support the vertical multistep coupling mechanism.

55 **Keywords:** Middle atmosphere, Secondary gravity wave, AIRS/Aqua, VIIR/Suomi-NPP, Andes,
56 Mountain wave

57 **1 Introduction**

58 Gravity waves (GWs) play an important role in driving atmospheric circulation, which
59 affects the temperature structure and distribution of chemical components (*Fritts and Alexander*,
60 2003; *Butchart et al.*, 2010). Mountain waves are one type of GW and are emitted from wind
61 flowing over a topography. Mountain waves transport a significant amount of momentum from
62 the lower to the middle atmosphere, a process that is typically parameterized in numerical
63 models (*Fritts and Alexander*, 2003; *Alexander et al.*, 2010; *Butchart et al.*, 2010). Mountain
64 waves have been studied using various observations, theoretical considerations, and numerical
65 simulations over the last few decades. Satellite observational instruments such as the
66 atmospheric infrared sounder (AIRS) (*Hoffmann et al.*, 2013; *Ern et al.*, 2017), microwave limb
67 sounder (MLS) (*Wu and Eckermann,* 2008), and sounding of the atmosphere using broadband
68 emission radiometry (SABER) (*Preusse et al.,* 2009)) have provided global maps of GW

2

69 activity. They have shown that the Andes are one of the most intense GW activity regions in the
70 middle atmosphere due to mountain waves caused by wind flowing over the Andes. The high
71 GW activity region extends leeward (or eastward) of the Andes due to the polar night jet (*Sato et*
72 *al.*, 2012).

73   Mountain waves theoretically have quasi-stationary ground-based phase velocity and
74 may encounter a critical level in weak wind layers (*Fritts and Alexander*, 2003). When GWs
75 break, they not only accelerate background circulation but also excite secondary GWs (*Vadas et*
76 *al.*, 2003; *Bacmeister and Schoeberl*, 1989; *Heale et al.*, 2020). A few observational studies have
77 shown statistically that secondary GWs are likely associated with mountain wave events over the
78 Andes. *de Wit et al.* (2017) estimated GW momentum flux over the Southern Andes using
79 meteor radar wind measurements and found a significant vertical flux of eastward momentum in
80 the mesosphere and lower thermosphere. GW sources in the troposphere cannot explain this
81 eastward momentum flux because a polar vortex is present over the Southern Andes. *de Wit et al.*
82 (2017) argued that secondary GWs contributed to this eastward momentum flux. *Liu et al.* (2019)
83 found high mountain wave activity in the Austral winter over the Andes up to altitudes of 55 km
84 that attenuated between 55-65 km of altitude. GW activity increased again above 65 km of
85 altitude with a westward tilt. Their results suggest that breaking mountain waves over the Andes
86 generate secondary GWs. However, to the best of our knowledge, no direct nadir simultaneous
87 observations of a mountain wave and the corresponding secondary wave have been reported.

88   Two mechanisms can generate secondary GWs: nonlinear fluid interactions and local
89 body forces (*Vadas and Becker.*, 2018; *Heale et al.*, 2020). Nonlinear interactions result in a
90 cascade of energy to smaller-scales and the generation of secondary GWs that have smaller
91 scales than those of the primary GWs (*Fritts et al.*, 1994; *Andreassen et al.*, 1998; *Fritts et al.*,
92 1998). *Bossert et al.* (2015) observed small-scale GWs in a warm phase front of a mountain
93 wave over Mount Cook, New Zealand by using Advanced Mesosphere Temperature Mapper
94 observations aboard an aircraft. *Heale et al.* (2017) simulated this event by using a 2-D nonlinear
95 model and found that secondary GWs were created in the warm phase where instabilities were
96 excited due to primary GWs breaking. The secondary GWs had smaller horizontal wavelengths
97 than the wavelength of the mountain wave by one order of magnitude and had broad phase
98 velocity spectra.

99   Alternatively, secondary GWs can also be created by local body forces such as
100 temporally and spatially localized wave drag, created by the deposition of momentum that
101 accompanes primary GW breaking. A local body force creates an imbalance in the flow so that
102 the resultant wave-mean flow interaction generates secondary GWs (*Vadas et al.*, 2003, 2018).
103 The latter secondary GW spectra have broad horizontal phase speeds, periods, and wavelengths,
104 and propagate in all azimuths except perpendicular to the body force direction. These spectra
105 depend on the size and duration of the local body force. Some secondary GWs can avoid
106 breaking or reaching critical levels over large distances and thus can "carry" momentum and
107 energy into the upper atmosphere. *Vadas et al.* (2003, 2018) simulated secondary GWs created
108 by a local body force using a Fourier-Laplace model. They found that the peaks of the horizontal
109 and vertical wavelength spectra were ~2 times larger than the horizontal and 1-2 times larger
110 than the vertical sizes of the local body force. In addition, the peak of the period spectrum was
111 the characteristic period of the body force unless the duration was longer.

112   *Vadas and Becker* (2019) showed that during a strong mountain wave event, the
113 mountain waves break near the stratopause, thereby generating secondary GWs from local body

3

114 forces. These secondary GWs then propagated higher, where they broke and dissipated at an
115 altitude between ~80-130 km, thereby creating tertiary GWs that propagated higher into the
116 thermosphere. Such higher-order GWs were likely observed by the GOCE satellite (*Vadas et al.,*
117 *2019*) as "hotspot" traveling atmospheric disturbances, (*Trinh et al.*, 2018), which was verified
118 by a recent modeling study (*Becker and Vadas*, JGR, submitted). Thus, this strongly suggests
119 that momentum and energy are transported into the upper thermosphere via a vertical multistep
120 coupling mechanism (see Figure 21 in *Vadas and Becker*, 2019).

121   Using a high-resolution model, *Vadas et al.* (2018) demonstrated that secondary GWs
122 have "fishbone structures" in vertical time slices, which indicates that secondary GWs radiate up
123 and down from primary GW breaking regions. They also found several fishbone structures near
124 the winter stratopause over McMurdo in lidar data. Secondary GWs from mountain wave
125 breaking over the Andes were simulated using a high-resolution, GW-resolving general
126 circulation model (*Becker and Vadas,* 2018). *Vadas and Becker* (2019) showed that secondary
127 GWs had concentric ring-like structures. A concentric ring-like GW was captured over Chile in
128 OH imager data, and no convection appeared near the OH imager site (*Vargas et al.*, 2016). They
129 inferred that the ring-like GW was generated by a primary GW breaking (possibly generated by
130 convection over Bolivia), although they did not capture the primary GW.

131   The purpose of this study is to provide the first direct observational evidence that ring-
132 like secondary GWs in the mesopause are created from mountain waves over the Andes, similar
133 to *Vadas and Becker* (2019). According to their model results, the strong eastward wind flowing
134 over the Andes creates mountain waves with large amplitudes, and the mountain waves
135 propagate upward and break at 50-80 km altitude. The momentum deposition that accompanies
136 this breaking process generates local body forces that excite secondary GWs with partial
137 concentric ring-like structures. Some of these secondary GWs then propagate to 100 km.
138 Observations from two satellite instruments, AIRS and the Visible/Infrared Imaging Radiometer
139 Suite (VIIRS), were used to capture both mountain waves and secondary GWs. AIRS can
140 observe GWs at an altitude range of approximately 20-50 km and observed mountain waves
141 during this event. VIIRS observes OH airglow intensity and captured secondary GWs with ring-
142 like structures at an altitude of ~87 km during this event.

143 **2 Satellite observations of gravity waves: AIRS and VIIRS**

144   2.1 Atmospheric Infrared Sounder (AIRS)
145   The AIRS instrument aboard the NASA Aqua satellite (*Aumann et al., 2003*; *Chahine et*
146 *al.,* 2006) measures infrared radiance spectra in three spectral bands between 3.74 and 15.4 μm.
147 The Aqua satellite was launched in 2002. Aqua has an orbit altitude of 705 km and an orbit
148 period of ~100 min, with local equatorial crossing times of ~1:30 PM and 1:30 AM. AIRS uses
149 cross-track scanning, with each scan consisting of 90 footprints over 1,780 km of ground
150 distance and a separation of 18 km of along-track distance. The footprint size varies between
151 $14 \times 14 \ km^2$ at nadir and $21 \times 42 \ km^2$ at the edges of the scan. AIRS measurements in the 4.3
152 and 15 μm CO_2 bands have been applied in various studies of stratospheric GWs. Here, 15 μm
153 brightness temperature data averaged over two sets of AIRS channels were used to investigate
154 mountain waves in the stratosphere. First, the brightness temperatures observed in multiple AIRS
155 channels were averaged to reduce the measurement noise. Two channel sets were used for
156 averaging, with temperature kernel functions peaking in two layers around ~23 and ~40 km of
157 altitude. The weighing functions have typical full widths at half maximum of ~15 km and

4

158   therefore represent mean temperatures over the altitude ranges of 17-32 and 34-49 km,
159   respectively. Second, a fourth-order polynomial fit was subtracted for each across-track scan to
160   remove the background temperatures. The remaining brightness temperature perturbations
161   provide a measure of GWs with vertical wavelengths longer than 10-15 km and horizontal
162   wavelengths longer than 30-80 km. The AIRS/Aqua observations of GWs are described in more
163   detail by *Hoffmann et al.* (2013, 2017).
164   2.2 Visible/Infrared Imaging Radiometer Suite (VIIRS)
165   The VIIRS instrument aboard the NOAA/NASA Suomi-NPP satellite, launched in 2011,
166   provides global coverage of visible and infrared wavelength spectra (*Miller et al.*, 2015). Its orbit
167   period and local equatorial crossing times are almost the same as Aqua's, but its orbit altitude is
168   834 km. VIIRS has 22 channels ranging between 0.41 and 12.01 μm. The day/night band (DNB)
169   sensor is one of the channels and can detect very faint light within 0.505-0.89 μm; therefore, the
170   DNB sensor can capture OH airglow intensity modulated by GWs at an altitude of ~87 km. The
171   horizontal spatial resolution and coverage of the DNB sensor is high ($0.74 \times 0.74\ km^2$ and a
172   3,000 km across-track swath width) and is preserved across the entire swath. Thus, the DNB
173   sensor can capture very small GWs with a horizontal wavelength of several kilometers. In terms
174   of the minimum vertical wavelength (λ_z) of GWs, the ability of the DNB to detect OH airglow
175   intensity modulation depends on the OH airglow thickness so the DNB can typically detect GWs
176   with $\lambda_z \geq 10$ km.
177   However, DNB also captures reflections from clouds. Tropospheric clouds frequently
178   have wave structures, which makes it difficult to distinguish them from GW modulations in the
179   OH airglow layer. The M15 band sensor is one of the 22 channels in VIIRS and can detect cloud
180   infrared brightness signals (9.8–11.8 μm). This sensor enables us to distinguish GW modulation
181   in the OH airglow layer from cloud reflections.
182

183   **3 AIRS and VIIRS observations of primary and secondary GWs**

184   3.1. GWs with strong amplitudes captured by AIRS on 24-25 July 2017
185   AIRS captured mountain waves with strong amplitudes over the Southern Andes on 24
186   July 2017, 18:32–18:42 UT and 25 July 2017, 05:43–05:53 UT. Figures 1 (a) and (b) show
187   brightness temperature perturbations at altitudes of ~23 and ~40 km on 24 July, respectively.
188   Figures 1 (c) and (d) show the perturbations at the same altitudes on 25 July. The GWs were
189   present directly above the Andes in both layers at both observation times, although the GWs on
190   25 July were further southward. The GW wavefronts were almost parallel to the Andes mountain
191   chain, which extends from 10°N to 55°S on the west side of the South American continent.
192   Figures 1 (e) and (f) show the horizontal wind at 2 km altitude at 12 UT on 24 July and at 0 UT
193   on 25 July, respectively. A mesoscale vortex-like pattern appears upwind of the Andes, and its
194   center is located around 100°W, 57°S at 12 UT on 24 July. Eastward tropospheric winds over
195   the Andes are strong (~20–40 m s^{-1}) in the northeast side of the vortex-like pattern. Such wind
196   conditions in the lower troposphere are favorable for the occurrence of a strong mountain wave
197   event (*Vadas and Becker*, 2019). A backward GW ray tracing simulation was performed with the
198   same model, initial GWs parameters, and background meteorogical conditions in Section 4. The
199   ray tracing result showed that the observed GW originated from the Andes, which suggests that
200   the GWs were mountain waves. The strong wind region over the Andes moved southward at 0
201   UT on 25 July, and the observed GWs also moved southward on 25 July in conjunction with the

202 strong wind (Figure 1 (f)). Thus, the observed GWs lasted at least ~11 h and were most likely
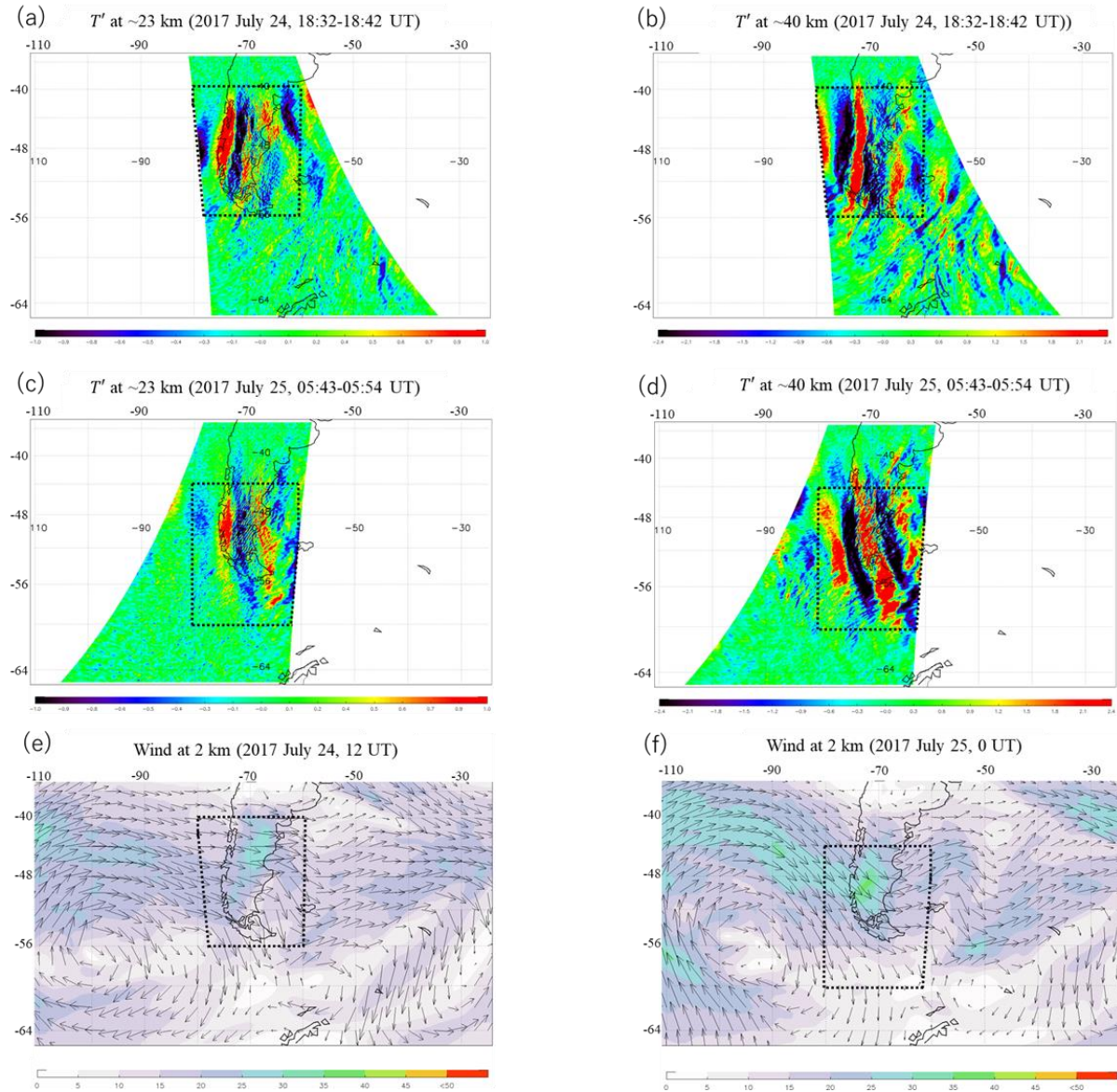203 mountain waves.
204

Figure 1. (a) and (b) show 15 μm brightness temperature perturbations from AIRS with GWs at
altitudes of ~23 and ~40 km at 18:32-18:42 UT on 24 July 2017, respectively. (c) and (d) show
the same as a and b, but at 05:43-05:54 on 25 July 2017. (e) and (f) show the MERRA-2 low-
level winds at an altitude of 2 km at 12 UT on 24 July and 0 UT on 25 July, respectively.

209

210   3.2. Concentric ring-like waves captured by VIIRS
211   Suomi-NPP passed over the Andes between 04:15-04:26 UT on 25 July 2017. Before this
212 time, mountain waves were present for many hours (Figure 1). Figure 2 (a) shows the OH
213 airglow perturbations where waves are present at $30—70°W, 48—64°S$. Their wavelengths are
214 approximately 100 km so the bandpass Butterworth filter with a cutoff at $50—220$ km was
215 applied to the OH intensity deviations to retrieve the wave structures (Figure 2 (b)). Many waves

216 overlap the leeward side of the Andes. The red dashed lines in Figure 2 (b) indicate some of
217 these waves. Most are curved structures. Figure 2 (c) shows the brightness temperatures from the
218 M15 channel at the same time as Figure 2 (a) and (b). Some wave-like cloud structures can be
219 seen in Figure 2 (c). The red dashed lines in Figure 2 (c) indicate examples of wave-like cloud
220 structures. The same structures are present in the OH intensity in Figure 2 (a) and (b) and are
221 therefore not created by GWs, but rather by reflections of clouds. However, the fine wave
222 structures extending leeward are not found in Figure 2 (c) and are therefore structures created by
223 GWs (i.e., the wavefronts indicated by the red dashed lines in Figure 2 (b)).
224   To the best of our knowledge, GWs with concentric ring-like structures can be created
225 from two mechanisms: secondary generation from temporally and spatially localized momentum
226 deposition (*Vadas et al.*, 2003, 2019) and deep convection (*Taylor and Hapgood*, 1988). One of
227 the main features of both mechanisms is a curved front, i.e., a partial concentric ring, which
228 appears in Figure 2(b). This allows the apparent centers of the concentric ring structure to be
229 determined. A concentric ring structure is distorted and moves leeward from the actual epicenter
230 of a wave and has been shown to occur when concentric GWs propagate in a strong wind (*Vadas
231 et al.*, 2009), and likely occurs here from the polar night jet. In the case of *Vadas et al.* (2009),
232 concentric GWs were created by deep convection. However, deep convection is unlikely to occur
233 at ~50°S during July, which is wintertime in the southern hemisphere, and there was no deep
234 convection in Figure 2 (c). In addition, a transmission diagram was calculated from MERRA-2
235 data in accordance with *Tomikwa* (2015) and shows that GWs with 80–120 km wavelengths and
236 east-to-south phase velocities hardly penetrated the stratosphere from the tropopause (not shown)
237 around the Southern Andes. Thus, the concentric ring-like GWs observed here are likely not
238 convective GWs. These ring-like GWs are probably secondary GWs generated by local body
239 forces created from mountain waves breaking in the stratosphere and the mesosphere, as
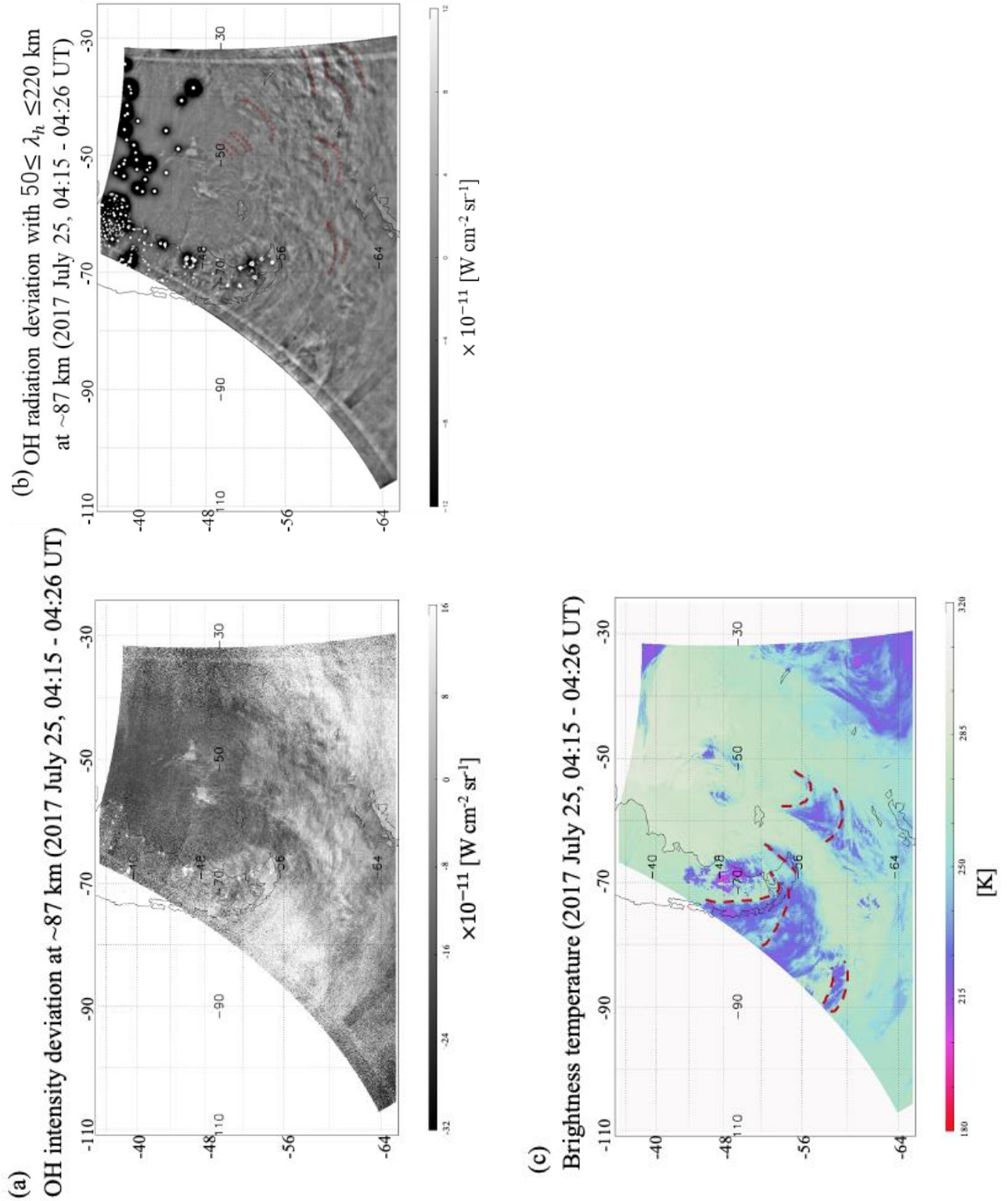240 discussed in the next section.
241
242
243
244

Figure 2. (a) OH intensity deviation at an altitude of ~87 km at 04:15-04:26 on 25 July 2017. (b) The same as in (a), but the deviations have been filtered with a bandpass filter allowing for wavelengths in the range of 50-220 km. (c) Brightness temperatures of clouds at the same time at 9.8-11.8 μm.

8

249

4 Mountain Waves Breaking

In our case study, the AIRS observations show mountain waves, and the VIIRS observations show concentric ring-like waves with multiple apparent centers leeward of the Andes (Figure 2 (b)). These features suggest that mountain waves propagate and break in the stratosphere or lower mesosphere, where they create local body forces. *Sato et al.* (2012) pointed out that MWs over the Andes preferentially propagate leeward due to refraction caused by wind shear of the polar night jet. Using a high-resolution GW-resolving global circulation model, *Vadas and Becker* (2019) demonstrated that local body forces caused by MWs breaking over the Andes extended leeward and southward at an altitude range of 50-80 km (Figures 8 and 9 in *Vadas and Becker* (2019)). *Vadas and Becker* (2019) also showed that these forces were located at the center of concentric ring-like GWs, which suggests that the concentric ring-like GWs are secondary GWs. Each body force excites secondary GWs with concentric ring-like structures, as shown in Vadas et al. (2018). The MWs over the Andes tend to break in the stratosphere or lower mesosphere at and above the altitude where the polar night is at a maximum during winter due to convective instability or critical level filtering (*Vadas and Becker*, 2019). However, weak-amplitude mountain waves can also propagate into the OH layer if no wind reversals occur (*Smith et al.*, 2009; *Bossert et al.*, 2015). Here, the VIIRS observations showed that stationary mountain waves were not present near the mesopause.

To estimate the paths of the mountain waves and their breaking/saturation locations or local body force locations, a forward GW ray tracing simulation was performed. Our ray tracing model is the same as that of *Kogure et al.* (2018), and its mathematical theory is based on *Marks and Eckerman* (1995) and *Dunkerton* (1984). The background wind and temperature were obtained from the MERRA-2 reanalysis. It should be noted that the MERRA-2 data between 0.1 and 0.01 hPa (altitude of ~68-75 km) are uncertain due to the upper boundary condition (*Gelaro et al.*, 2017). The background fields were defined as mean values from 18 UT on 24 July to 06 UT on 25 July, the period during which the mountain waves were observed. The ground-based initial period of the mountain waves was assumed to be 0 s because the mountain waves are approximately stationary (*Dunkerton*, 1984), and the sign of their vertical group velocity is upward. The initial altitude for the mountain waves was assumed to be 40 km, which is the most sensitive altitude of the weighting functions for the AIRS brightness temperature observations. The initial horizontal wave vectors were derived from AIRS brightness temperature perturbations. The perturbations in the dashed frame in Figure 2 (b) were analyzed using the Lomb–Scargle method (*Scargle* 1982) to derive a 2D Lomb–Scargle periodogram. The wavenumber at the maximum power is $1.2 \times 10^{-2} km^{-1}$, which corresponds to a wavelength of ~520 km and was used as the initial value. The azimuthal angles of the wave vectors at the power maximum are 86° and 266° clockwise from north. It should be noted that the azimuthal angle has an 180° ambiguity due to the 2D spectral analysis. However, the propagation direction of a mountain wave is opposite to the background wind over a surface obstacle (*Nappo*, 2002). The eastward wind at 2 km altitude over the Andes mountain chain (Figure 2 (e, f)) is eastward; thus, 266° was chosen for the initial azimuthal angle. Gravity wave ray tracing was conducted at 9 points ($70° \pm 8°W, 48° \pm 8°S$).

GWs break when they reach critical levels or when they become unstable. These instabilities are classified into two types: shear instability and convective instability. Our ray tracing analysis can estimate the locations for critical levels of mountain waves, but cannot

9

294   identify locations of instabilities caused by mountain waves. To investigate the occurrence of the
295   instabilities of the mountain waves, the Richardson number, R_i, and the ratio between the
296   horizontal wind amplitude (u'_{amp}) and the intrinsic horizontal phase speed (c) were estimated
297   along the ray path of each mountain wave. When R_i is less than 0.25, this indicates the
298   likelihood of shear instability (*Fritts and Alexander*, 2003). Convective instability is possible
299   when the ratio u'_{amp}/c is larger than 0.7-1 (Vadas and Becker, 2019). In accordance with Vadas
300   and Becker (2019), the threshold for the ratio was 0.7. The temeprature amplitude, T'_{amp}, at the
301   initial altitude (40 km altitude) were derived from the variance of the brightness temperature in
302   the dashed frame in Figure 2 (b). In this case, T'_{amp} is 3 K. u'_{amp} was estimated with the
303   assumption of inrtial GW by equation (10) in *Geller and Gong* (2010). The T'_{amp} and u'_{amp}
304   values at the altitude of the next step was calculated from the total GW energy, assuming that the
305   energy increases with an e-folding at twice the density scale height (*Alexander et al.*, 2011;
306   *Kogure et al.*, 2017; *Liu et al.*, 2014; *Lu et al.*, 2015).
307
308   Figure 3 shows the ray paths of the mountain waves superimposed on Figure 2 (b).
309   Triangles indicate where the waves may have encountered shear instability. Almost all waves
310   encountered critical levels at altitudes of ~60 km, except for two waves that originated at
311   $70°W, 56°S$ and $62°W, 56°S$. These two waves reached the model top (~75 km) of MERRA-2.
312   All waves had a preference to propagate leeward. Moreover, all waves began to meet the shear
313   instability condition at altitudes of ~60 km. Most waves began to meet the convective instability
314   condition a few kilometers higher in altitude than those of the shear instability condition.
315   However, one wave that originated at $62°W, 56°S$ met the convective instability condition at ~10
316   km higher altitude (~72 km) and two waves originating at $70°W, 56°S$ and $77°W, 56°S$ did not
317   meet the condition (not shown). Since brightness temperature variances observed by AIRS are
318   typically much smaller than the actual atmospheric temperature variance (*Hoffmann et al.*, 2014),
319   these waves possibly met the conditions at lower altitudes than those in our ray tracing results.
320   These results indicate that the mountain waves propagated to the region where the concentric
321   ring-like GWs appeared, and then they broke. This result is consistent with the model study of
322   *Vadas and Becker* (2019).
323   It should be noted that the centers of some concentric ring-like GWs (around $35°E, 60°S$)
324   are far (~1000 km) from the edge of the ray tracing results ($55°E, 56°S$). This horizontal distance
325   could be explained by two possibilities. One possibility is that background horizontal wind above
326   the observable altitude of AIRS accelerated rapidly in the eastward direction in time. This would
327   cause the MWs to be swept thousands of kilometers downstream before breaking (*Vadas and
328   Becker*, 2018). Such acceleration would not be captured by the MERRA-2 winds. Another
329   possibility is that some mountain waves were present further leeward in the stratosphere than the
330   waves captured by AIRS. A mountain wave with a larger perpendicular component to the zonal
331   wind of its wave vector over the Andes has a preference to propagate leeward (*Sato et al.*, 2012).
332   Such a mountain wave should have a small vertical wavelength because the vertical wavelength
333   of a mountain wave is proportional to a parallel component of a background wind (*Nappo*,
334   2002). Since AIRS cannot detect GWs with vertical wavelengths less than ~12 km, it is possible
335   that AIRS failed to detect these mountain waves in the leeward direction, although the mountain
336   waves broke and created the concentric ring-like waves seen by VIIRS.
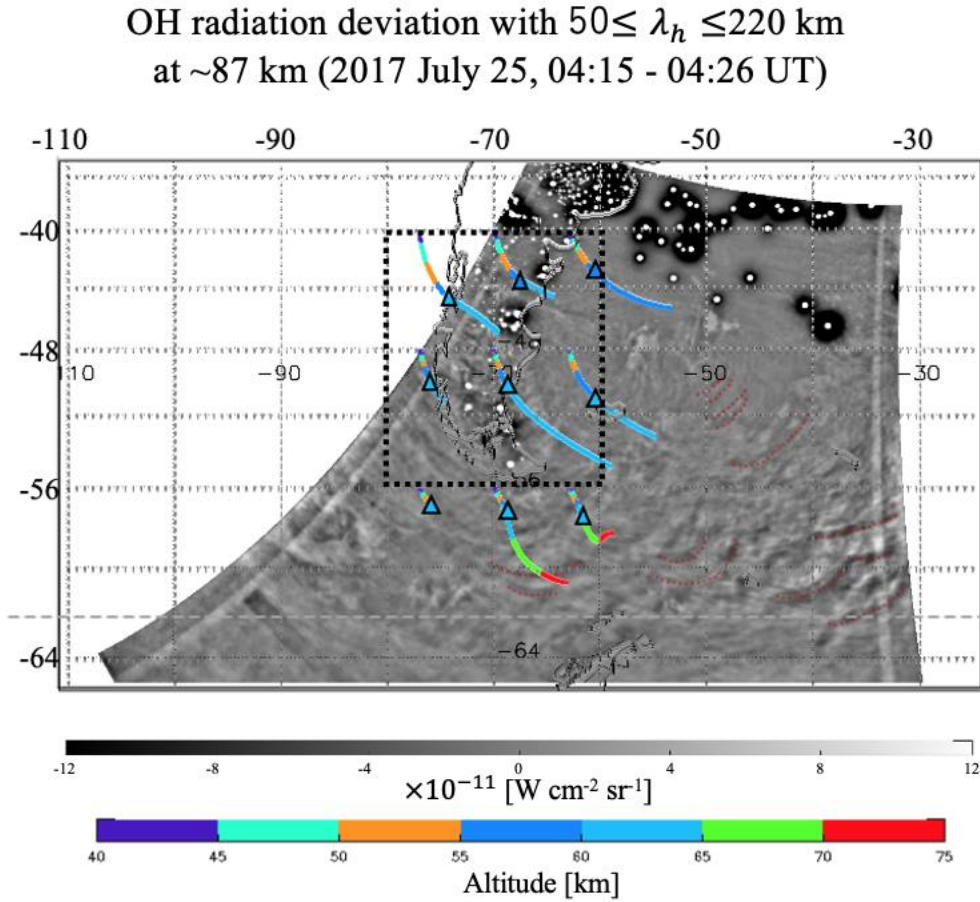337
338

10

339
340

Figure 3. The ray tracing results are superimposed on Figure 2b. The colors indicate the altitude of each mountain wave. The triangles indicate the estimated locations of shear instability.

Thus, we conclude that the concentric ring-like GWs observed here were likely secondary GWs caused by local body forces from breaking mountain waves. These results are the first direct observational evidence for a similar phenomenon simulated by *Vadas and Becker* (2019) where mountain waves over the Andes create secondary GWs with a concentric ring-like structure. However, the horizontal wavelengths of the observed secondary GWs (~100 km) were much shorter than those in their model (500-2000 km). The inconsistency between the observations and the model could be due to the fact that the minimum horizontal wavelength resolvable by *Vadas and Becker* (2019) was ~165 km (i.e., the model had a horizontal grid spacing of ~65 km). This implies that their model cannot simulate the small-scale concentric GWs observed by VIIRS. Additionally, GWs are only observable in the OH layer if they have vertical wavelengths > 10 km (*Liu and Swenson,* 2003). Since the secondary GW spectrum excited by a local body force is quite broad (Vadas *et al.*, 2003) and many of the large-scale secondary GWs observed in *Vadas and Becker* (2019) have smaller vertical wavelengths, it is possible that they were not seen in the OH airglow layer. Finally, although VIIRS can potentially capture GWs with ~1000 km horizontal wavelengths because of its wide field of view, portions of the VIIRS images are frequently contaminated with clouds or city lights, making it difficult to

11

361 capture large-scale GWs. Thus, VIIRS tends to be sensitive to secondary GWs with smaller
362 horizontal wavelengths than those in the *Vadas and Becker* (2019) model.

5 Conclusion

364   AIRS captured a mountain wave event with significant brightness temperature amplitudes
365 (3 K) in the stratosphere and ~500 km horizontal wavelengths over the Southern Andes on 24-25
366 July 2017. During this event, VIIRS did not detect mountain waves but instead observed
367 concentric ring-like GWs with ~100 km wavelengths at 04:30 UT on the same night leeward of
368 the Southern Andes. Our ray tracing result shows that the mountain waves propagated to the east
369 where the concentric GWs appeared while the mountain waves were breaking. Thus, the
370 concentric waves were probably secondary GWs generated by local body forces created by the
371 breaking mountain waves. These observational results are consistent with the model results of
372 *Vadas and Becker* (2019), except for the horizontal wavelengths of the secondary GWs. This
373 difference in horizontal wavelengths could be due to differing coverage of the GW spectrum
374 between the VIIRS observations and the model. This study shows the first concrete evidence that
375 secondary GWs are generated by mountain waves over the Andes and have concentric or ring-
376 like structures. In addition, this study supports the theory of *Vadas and Becker* (2019) for vertical
377 coupling via secondary and higher-order GWs throughout the middle and upper atmosphere.

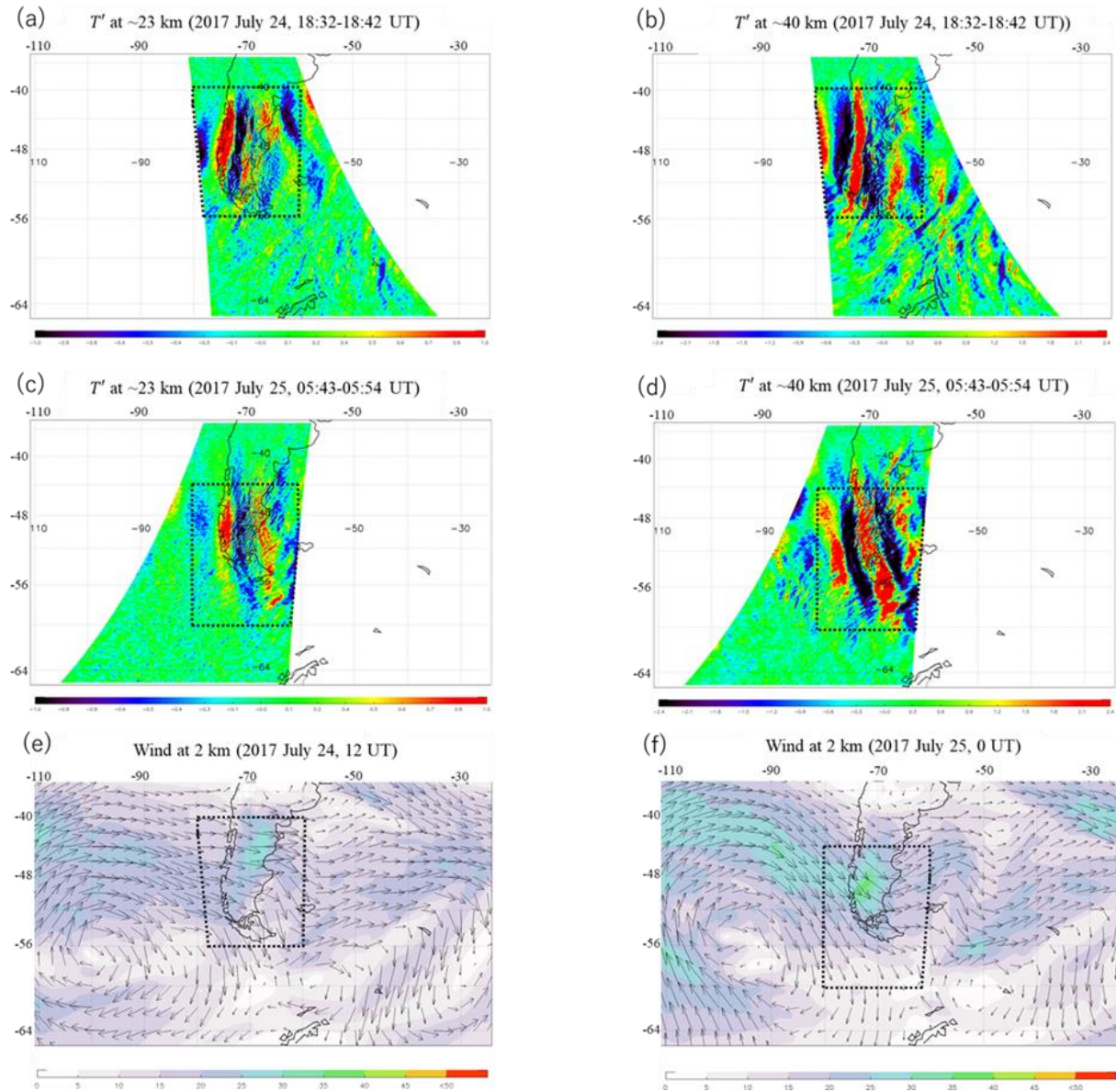## Acknowledgments, Samples, and Data

389

References

391 Alexander, M.J., Geller, M., McLandress, C., Polavarapu, S., Preusse, P., Sassi, F., et al. (2010).
392   Recent developments in gravity-wave effects in climate models and the global
393   distribution of gravity-wave momentum flux from observations and models. *Quarterly*
394   *Journal of the Royal Meteorological Society*, 136: 1103–1124. doi:10.1002/qj.637

395 Alexander, S. P., Klekociuk, A. R., & Murphy, D. J. (2011). Rayleigh lidar observations of
396   gravity wave activity in the winter upper stratosphere and lower mesosphere above
397   Davis, Antarctica (69°S, 78°E). *Journal of Geophysical Research*, 116, D13109.
398   doi:10.1029/2010JD015164

399 Andreassen, Ø, Hvidsten, P., Fritts, D., & Arendt, S. (1998). Vorticity dynamics in a breaking
400   internal gravity wave. Part 1. Initial instability evolution. *Journal of Fluid Mechanics,*
401   367, 27–46. doi:10.1017/S0022112098001645

Aumann, H. H., Chahine, M. T., Gautier C., Goldberg, M. D., Kalnay E., McMillin, L. M., et al (2003). AIRS/AMSU/HSB on the Aqua mission: Design, science objectives, data products, and processing systems. *IEEE Transactions on Geoscience and Remote Sensing*, *41*(2), 253–264.

Bacmeister, J. T., & Schoeberl, M. R. (1989). Breakdown of Vertically Propagating Two-Dimensional Gravity Waves Forced by Orography. *Journal of the Atmospheric Sciences,* 46, 2109–2134. doi:10.1175/1520-0469(1989)046<2109:BOVPTD>2.0.CO;2

Becker, E., & Vadas S. L. (2018). Secondary gravity waves in the winter mesosphere: Results from a high-resolution global circulation model. *Journal of Geophysical Research: Atmospheres*, 123. doi:10.1002/2017JD027460

Becker, E., & Vadas S. L. (2020). Explicit global simulation of gravity waves in the thermosphere, submitted to *Journal of Geophysical Research: Space Physics*.

Bossert, K., Fritts, D. C., Pautet, P.-D., Williams, B. P., Taylor, M. J., Kaifler, B., et al. (2015). Momentum flux estimates accompanying multiscale gravity waves over Mount Cook, New Zealand, on 13 July 2014 during the DEEPWAVE campaign. *Journal of Geophysical Research: Atmospheres*, 120, 9323–9337. doi:10.1002/2015JD023197

Butchart, N., Cionni, I., Eyring, V., Shepherd, T. G., Waugh, D. W., Akiyoshi, H., et al. (2010). Chemistry–Climate Model Simulations of Twenty-First Century Stratospheric Climate and Circulation Changes. *Journal of Climate*, 23, 5349–5374. doi:10.1175/2010JCLI3404.1

Chahine, M. T., Pagano, T. S., Aumann, H. H., Atlas, R., Barnet, C., Blaisdell, J., et al. (2006). AIRS: Improving Weather Forecasting and Providing New Data on Greenhouse Gases. *Bulletin of the American Meteorological Society,* 87,911–926. doi:10.1175/BAMS-87-7-911

de Wit, R. J., Janches, D., Fritts, D. C., Stockwell, R. G., & Coy, L. (2017). Unexpected climatological behavior of MLT gravity wave momentum flux in the lee of the Southern Andes hot spot. *Geophysical Research Letters*, 44, 1182–1191. doi:10.1002/2016GL072311.

Dunkerton, T.J., (1984). Inertia–Gravity Waves in the Stratosphere. *Journal of the Atmospheric Sciences,* 41, 3396–3404. doi:10.1175/1520-0469(1984)041<3396:IWITS>2.0.CO;2

Ern, M., Hoffmann, L., & Preusse, P. (2017). Directional gravity wave momentum fluxes in the stratosphere derived from high-resolution AIRS temperature data. *Geophysical Research Letters*, 44, 475–485. doi:10.1002/2016GL072007

Fritts, D. C., Isler, J. R., & Andreassen, Ø. (1994). Gravity wave breaking in two and three dimensions: 2. Three-dimensional evolution and instability structure. *Journal of Geophysical Research*, 99(D4), 8109– 8123. doi:10.1029/93JD03436

Fritts, D. C., Arendt S., & Anderassen, Ø. (1998). Vorticity dynamics in a breaking internal gravity wave. Part 2. Vortex interactions and transition to turbulence. *Journal of Fluid Mechanics*, 367, 47-65. doi:10.1017/S0022112098001633

Fritts, D. C., & Alexander, M. J. (2003). Gravity wave dynamics and effects in the middle atmosphere. *Reviews of Geophysics*, 41, 1003. doi:10.1029/2001RG000106, 1

13

443 Gelaro, R., McCarty, W., Suárez, M. J., Todling, R., Molod, A., Takacs, L., et al. (2017). The
444   Modern-Era Retrospective Analysis for Research and Applications, Version 2 (MERRA-
445   2). *Journal of Climate,* 30, 5419–5454. doi.org/10.1175/JCLI-D-16-0758.1

446 Geller, M. A., & Gong, J. (2010). Gravity wave kinetic, potential, and vertical fluctuation
447   energies as indicators of different frequency gravity waves. *Journal of Geophysical*
448   *Research*, 115, D11111. doi:10.1029/2009JD012266

449 Heale, C. J., Bossert, K., Snively, J. B., Fritts, D. C., Pautet, P.-D., & Taylor, M.
450   J. (2017), Numerical modeling of a multiscale gravity wave event and its airglow
451   signatures over Mount Cook, New Zealand, during the DEEPWAVE campaign, *Journal*
452   *of Geophysical Research: Atmospheres,* 122, 846–860. doi:10.1002/2016JD025700

453 Heale, C. J., Bossert, K., Vadas, S. L., Hoffmann, L., Dörnbrack, A., Stober, G., J. B. Snively, &
454   C. Jacobi (2020). Secondary gravity waves generated by breaking mountain waves over
455   Europe. *Journal of Geophysical Research: Atmospheres*, 125, e2019JD031662.
456   doi:10.1029/2019JD031662

457 Hoffmann, L., Xue, X., & Alexander, M. J. (2013). A global view of stratospheric gravity wave
458   hotspots located with Atmospheric Infrared Sounder observations. *Journal of*
459   *Geophysical Research: Atmospheres*, 118, 416– 434. doi:10.1029/2012JD018658

460 Hoffmann, L., Alexander, M. J., Clerbaux, C., Grimsdell, A. W., Meyer, C. I., Rößler, T., &
461   Tournier, B., (2014). Intercomparison of stratospheric gravity wave observations with
462   AIRS and IASI. *Atmospheric Measurement Techniques*, 7, 4517–4537.
463   doi.org/10.5194/amt-7-4517-2014

464 Hoffmann, L., Spang, R., Orr, A., Alexander, M. J., Holt, L. A., & Stein, O., (2017). A decadal
465   satellite record of gravity wave activity in the lower stratosphere to study polar
466   stratospheric cloud formation. *Atmospheric Chemistry and Physics*, 17, 2901–2920.
467   doi:10.5194/acp-17-2901-2017

468 Kogure, M., Nakamura, T., Ejiri, M. K., Nishiyama, T., Tomikawa, Y., & Tsutsumi,
469   M. (2018). Effects of horizontal wind structure on a gravity wave event in the middle
470   atmosphere over Syowa (69°S, 40°E), the Antarctic. *Geophysical Research*
471   *Letters*, 45, 5151–5157. doi:10.1029/2018GL078264

472 Kogure, M., Nakamura, T., Ejiri, M. K., Nishiyama, T., Tomikawa, Y., Tsutsumi, M., et al.
473   (2017). Rayleigh/Raman lidar observations of gravity wave activity from 15 to 70 km
474   altitude over Syowa (69°S, 40°E), the Antarctic. *Journal of Geophysical Research:*
475   *Atmospheres*, 122, 7869–7880. doi:10.1002/2016JD026360

476 Liu, A. Z., & Swenson, G. R. (2003). A modeling study of O_2 and OH airglow perturbations
477   induced by atmospheric gravity waves. *Journal of Geophysical Research*, 108, 4151.
478   doi:10.1029/2002JD002474, D4

479 Liu, X., Yue, J., Xu, J., Wang, L., Yuan, W., Russell, J. M., & Hervig, M. E. (2014). Gravity
480   wave variations in the polar stratosphere and mesosphere from SOFIE/AIM temperature
481   observations. *Journal of Geophysical Research: Atmospheres*, 119, 7368–7381.
482   doi:10.1002/2013JD021439

483 Lu, X., Chu, X., Fong, W., Chen, C., Yu, Z., Roberts, B. R., & McDonald, A. J. (2015). Vertical
484   evolution of potential energy density and vertical wave number spectrum of Antarctic

485   gravity waves from 35 to 105 km at McMurdo (77.8°S, 166.7°E). *Journal of Geophysical*
486   *Research: Atmospheres*, 120, 2719–2737. doi:10.1002/2014JD022751

487   Liu, X., Xu, J., Yue, J., Vadas, S. L., & Becker, E. (2019). Orographic primary and secondary
488   gravity waves in the middle atmosphere from 16-year SABER observations. *Geophysical*
489   *Research Letters*, 46, 4512–4522. doi:10.1029/2019GL082256

490   Marks, C. J., & Eckermann, S.D. (1995). A Three-Dimensional Nonhydrostatic Ray-Tracing
491   Model for Gravity Waves: Formulation and Preliminary Results for the Middle
492   Atmosphere. *Journal of the Atmospheric Sciences,* **52**, 1959–1984. doi:10.1175/1520-
493   0469(1995)052<1959:ATDNRT>2.0.CO;2

494   Miller D. S., William C. S., Jia Y., Steven M. S., Alexander, M. J., Lars H., et al. (2015). Upper
495   atmospheric gravity wave details revealed in nightglow satellite imagery. *Proceedings of*
496   *the National Academy of Sciences* 112 (49) E6728-E6735. doi: 10.1073/pnas.1508084112

497   Nappo, C. J. (2002), *An Introduction to Atmospheric Gravity Waves*. *Academic Press*, 260.

498   Preusse, P., Eckermann, S. D., Ern, M., Oberheide, J., Picard, R. H., Roble, R. G., et al.
499   (2009). Global ray tracing simulations of the SABER gravity wave climatology. *Journal*
500   *of Geophysical Research*, 114, D08126. doi:10.1029/2008JD011214

501   Sato, K., Tateno, S., Watanabe, S., & Kawatani, Y. (2012). Gravity Wave Characteristics in the
502   Southern Hemisphere Revealed by a High-Resolution Middle-Atmosphere General
503   Circulation Model. *Journal of the Atmospheric Sciences,* 69, 1378–
504   1396. doi:10.1175/JAS-D-11-0101.1

505   Sato, K., & Yoshiki, M. (2008). Gravity Wave Generation around the Polar Vortex in the
506   Stratosphere Revealed by 3-Hourly Radiosonde Observations at Syowa Station. *Journal*
507   *of the Atmospheric Sciences,* 65, 3719–3735. doi:10.1175/2008JAS2539.1

508   Smith, S., Baumgardner, J., & Mendillo, M. (2009). Evidence of mesospheric gravity-waves
509   generated by orographic forcing in the troposphere. *Geophysical Research Letters*, 36,
510   L08807. doi:10.1029/2008GL036936

511   Taylor, M. J., & Hapgood, M. A. (1988), Identification of a thunderstorm as a source of short
512   period gravity waves in the upper atmospheric nightglow emissions, *Planetary and space*
513   *science*, 36(10), 975–985. doi:10.1016/0032-0633(88)90035-9

514   Tomikawa, Y. (2015). Gravity wave transmission diagram. Ann. Geophys., 33, 1479–1484.
515   doi.org/10.5194/angeo-33-1479-2015

516   Trinh, Q. T., M. Ern, E. Doornbos, P. Preusse, & M. Riese (2018). Satellite observations of
517   middle atmosphere-thermosphere vertical coupling by gravity waves. Annals of
518   *Geophysics*, 36, 425–444. doi:10.5194/angeo-36-425-2018

519   Vadas, S. L., Fritts, D. C., & Alexander M. J. (2003). Mechanism for the Generation of
520   Secondary Waves in Wave Breaking Regions. *Journal of the Atmospheric*
521   *Sciences,* 60, 194–214. doi:10.1175/1520-0469(2003)060<0194:MFTGOS>2.0.CO;2

522   Vadas, S. L, Jia Y., Joe S., Pete S., & Alan L., (2009). A model study of the effects of winds on
523   concentric rings of gravity waves from a convective plume near Fort Collins on 11 May
524   2004. *Journal of Geophysical Research,* 114, D06103. doi:10.1029/2008JD010753

525   Vadas, S. L., Yue J., & Nakamura T., (2012). Mesospheric concentric gravity waves generated
526   by multiple convection storms over the North America Great Plain. *Journal of*
527   *Geophysical Research*, 117, D7. doi:10.1029/2011JD017025

528   Vadas, S. L., & Becker, E.(2018). Numerical modeling of the excitation, propagation, and
529   dissipation of primary and secondary gravity waves during wintertime at McMurdo
530   Station in the Antarctic. *Journal of Geophysical Research: Atmospheres*, 123, 9326–
531   9369. doi:10.1029/2017JD027974

532   Vadas, S. L., Zhao, J., Chu, X., & Becker E., (2018). The excitation of secondary gravity
533   waves from local body forces: Theory and observation. *Journal of Geophysical*
534   *Research: Atmospheres*, 123, 9296–9325. doi:10.1029/2017JD027970

535   Vadas, S. L., & Becker, E. (2019). Numerical modeling of the generation of tertiary gravity
536   waves in the mesosphere and thermosphere during strong mountain wave events over the
537   Southern Andes. *Journal of Geophysical Research: Space Physics*, 124, 7687–
538   7718. doi:10.1029/2019JA026694

539   Vadas, S. L., Xu, S., Yue, J., Bossert, K., Becker, E., & Baumgarten, G., (2019). Characteristics
540   of the Quiet-time Hotspot Gravity Waves Observed by GOCE over the Southern Andes
541   on 5 July 2010. *Journal of Geophysical Research: Space Physics*, 124, 7034–7061.
542   doi.org/10.1029/2019JA026693

543   Vargas, F., Swenson, G., Liu, A., & Pautet, D. (2016). Evidence of the excitation of a ring-like
544   gravity wave in the mesosphere over the Andes Lidar Observatory. *Journal of*
545   *Geophysical Research: Atmospheres*, 121, 8896–8912. doi:10.1002/2016JD024799

546   Wu, D. L., & Eckermann, S. D. (2008). Global Gravity Wave Variances from Aura MLS:
547   Characteristics and Interpretation. *Journal of the Atmospheric Sciences*, 65, 3695–3718.
548   doi:org/10.1175/2008JAS2489.1

549

550

551

552 **Figure 1**.

553
554 Figures 1. (a) and (b) show brightness temperature perturbations with GWs at altitudes of ~23
555 and ~40 km in 18:32-18:42 on 24 July 2017, respectively. (c) and (d) show the same as a and b,
556 respectively, but in 05:43-05:54 on 25 July 2017. (e) and (f) show wind at an altitude of 2 km at
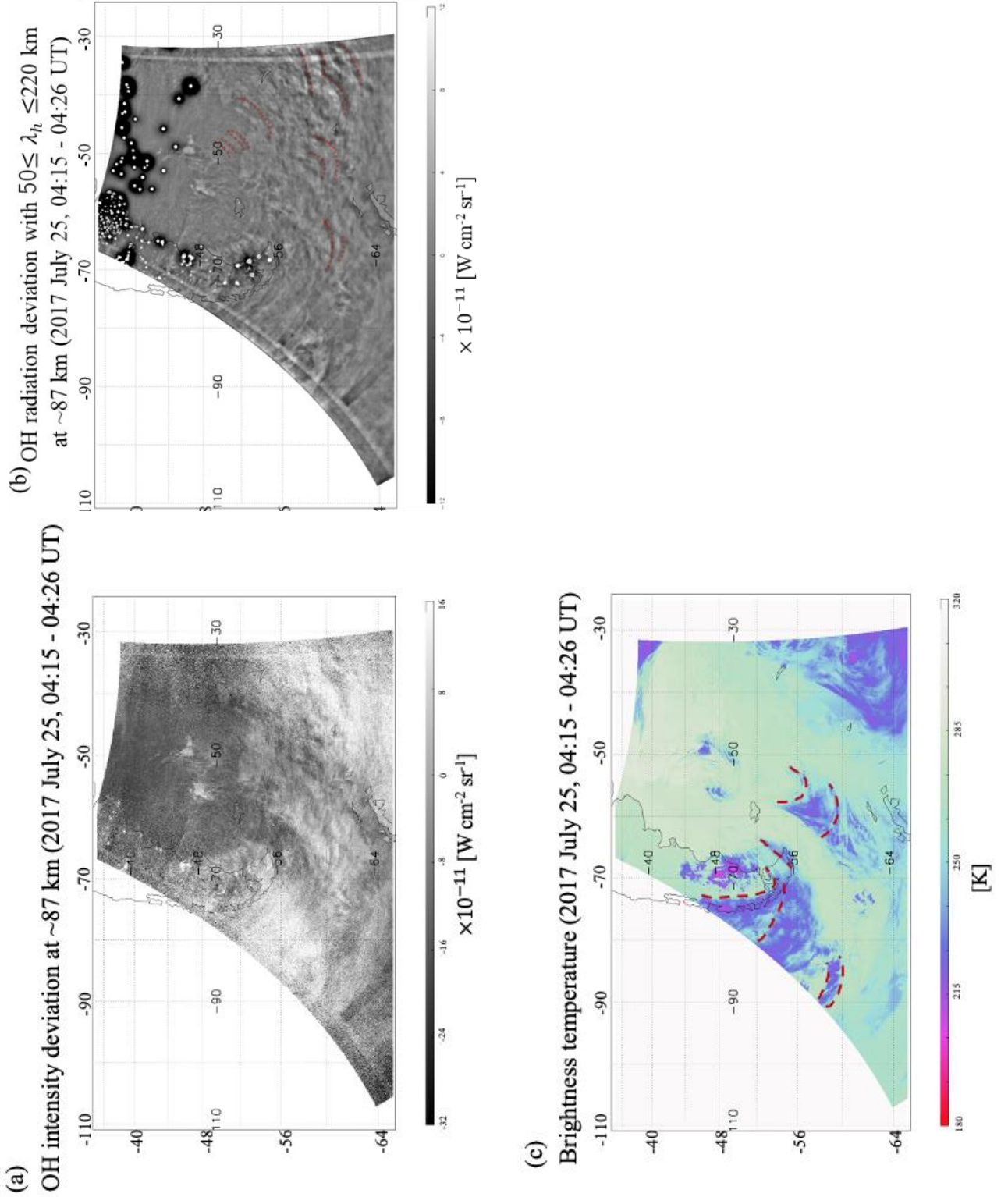557 12 UT on 24 July and 0 UT on 25 July, respectively.
558

17

Figure 2. (a) An OH intensity deviation at an altitude of ~87 km in 04:15-04:26 on 25 July 2017.
(b) The same as (a), but the deviation is applied with a bandpass filter. (c) shows brightness
temperatures of clouds at 9.8-11.8 μm.
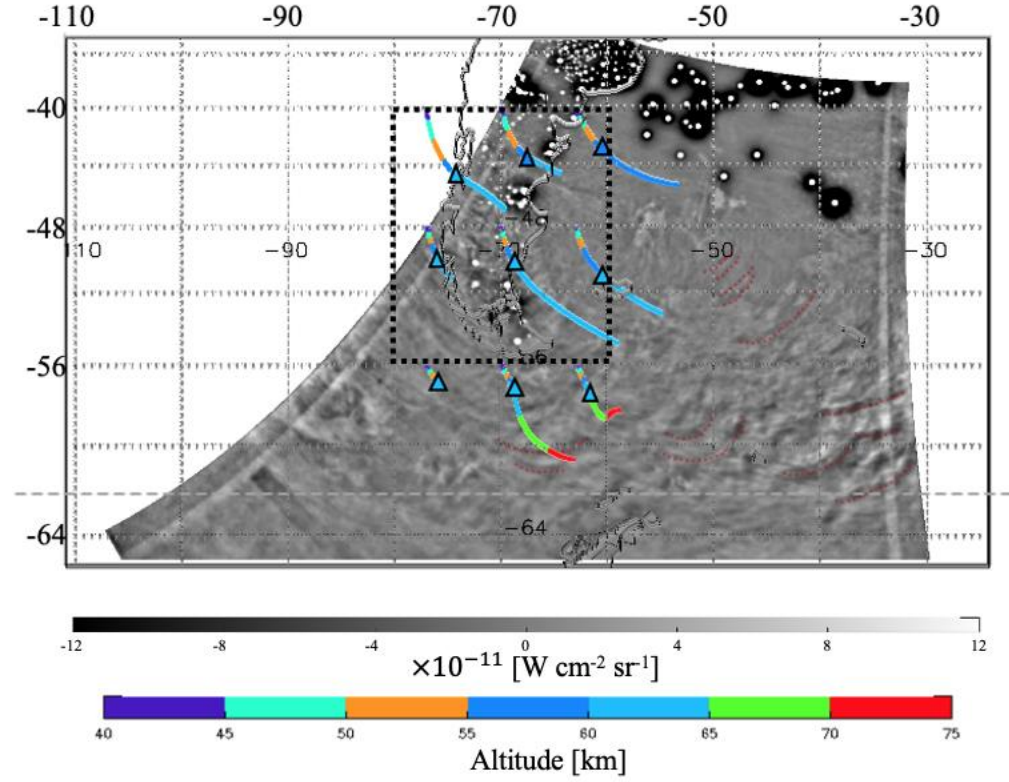
18

562 **Figure 3.**

563

564 Figure 3. The ray tracing results are superimposed in Figure 2b. These colors indicate the altitude
565 of each mountain wave. The squares indicate the beginning point of a shear instability.
566

19

567
568
569
570